*J. Fluid Mech.* (2011), *vol.* 677, *pp.* 179–203.  
doi:10.1017/jfm.2011.75

# New perspectives on the impulsive roughness-perturbation of a turbulent boundary layer

I. JACOBI† AND B. J. MCKEON

Graduate Aerospace Laboratories, California Institute of Technology, Pasadena, CA 91125, USA

(Received 7 September 2010; revised 27 December 2010; accepted 9 February 2011; first published online 26 April 2011)

The zero-pressure-gradient turbulent boundary layer over a flat plate was perturbed by a short strip of two-dimensional roughness elements, and the downstream response of the flow field was interrogated by hot-wire anemometry and particle image velocimetry. Two internal layers, marking the two transitions between rough and smooth boundary conditions, are shown to represent the edges of a 'stress bore' in the flow field. New scalings, based on the mean velocity gradient and the third moment of the streamwise fluctuating velocity component, are used to identify this 'stress bore' as the region of influence of the roughness impulse. Spectral composite maps reveal the redistribution of spectral energy by the impulsive perturbation – in particular, the region of the near-wall peak was reached by use of a single hot wire in order to identify the significant changes to the near-wall cycle. In addition, analysis of the distribution of vortex cores shows a distinct structural change in the flow associated with the perturbation. A short spatially impulsive patch of roughness is shown to provide a vehicle for modifying a large portion of the downstream flow field in a controlled and persistent way.

**Key words:** turbulent boundary layers

## 1. Background

Zero-pressure-gradient turbulent boundary-layer flow over a flat plate has been studied extensively and significant progress has been made towards a conceptual understanding of the structure and evolution of turbulence. Near the wall, a process of ejections and sweeps of fluid, often described as a bursting phenomenon, is thought to contribute significantly to the production of turbulence. These ejection and sweep motions constitute a near-wall cycle of fluid motions that have a controlling influence on the Reynolds stress near the wall and are closely associated with vortex structures located throughout the wall region, as reported by Hamilton, Kim & Waleffe (1995) and Jiménez & Pinelli (1999). Much of this same general framework applies equally to the case of a uniformly rough flat plate; however, roughness is thought to alter the mechanics of fluid entrainment and ejection at the wall – producing a more violent entrainment and nearly vertical ejection due to roughness geometry. Thus, Jiménez (2004) reports that the rough wall condition permanently disturbs the buffer-layer viscous cycle of the corresponding smooth wall. Both of these well-studied flow

† Email address for correspondence: jacobi@caltech.edu

situations present an equilibrium turbulent boundary layer, where the flow can be described entirely in terms of local turbulent processes. The less studied problem of non-equilibrium boundary layers, which depend on non-local factors, is acutely interesting because of the insight it potentially offers into the dynamic processes of the evolution of turbulent structure, as discussed by Morrison (2010). In addition, these non-equilibrium situations are of significant practical interest as shown by Smits & Wood (1985), with relevance to pipes, wings or other flow surfaces over which surface roughness and other properties change passively, and also in which control systems are designed to actively perturb flows. In the current study, the non-equilibrium behaviour produced by roughness changes is considered, both for its ubiquity in practical flows and its potential applicability to control strategies.

Flow over a surface which transitions between a rough and smooth boundary condition offers a simple and practically relevant case for non-equilibrium on a flat plate. For the transition from a smooth to rough surface ($S \rightarrow R$) studied by Antonia & Luxton (1971*a*), the return to equilibrium was monitored by the development of an internal layer corresponding to the adjustment of the flow to the new boundary condition, which started at the roughness transition point and grew quickly to the edge of the boundary layer itself, thereby reestablishing equilibrium in the flow field. The transition from a rough to smooth wall condition ($R \rightarrow S$) showed significantly slower growth of the corresponding internal layer, and the restoration of equilibrium was not observed even $16\delta$ downstream in a second experimental study by Antonia & Luxton (1972), where $\delta$ refers to the mean boundary layer thickness measured at 99% of the free stream velocity. Subsequently, the problem of a spatial impulse of roughness on an otherwise smooth boundary was considered by Andreopoulos & Wood (1982), since it provided an opportunity to isolate the influence of the roughness in a patch short enough to avoid establishment of equilibrium. In this way, the additional length scale of the roughness was introduced to the turbulent boundary layer and the response of the boundary layer could be observed downstream independent of the continued presence of the roughness itself. The growth of two internal layers, one from each boundary transition, was observed to be consistent with their independent growth rates, but other features of the flow indicated a nonlinear response to the impulse, and the overall recovery was dominated by the $R \rightarrow S$ transition.

Andreopoulos & Wood (1982), borrowing the language of Smits, Young & Bradshaw (1979), identified a propagating peak of Reynolds shear and normal stresses, downstream of the impulse, as a 'stress bore' – showing that the stress behaviour in non-equilibria due to changes in geometry shares key features in common with that of roughness-based non-equilibria. This peak was located between the two internal layers, which mark the mean domain of influence of the perturbation, and just as the second internal layer persisted even far downstream of the perturbation, so too the stress bore left an impression on the flow field even far downstream. Pearson, Elavarasan & Antonia (1997), in a similar experiment, although at significantly lower Reynolds number based on momentum thickness, $\theta$ ($Re_\theta \approx 1400$ compared to Andreopoulos & Wood's $Re_\theta = 4300$–$7600$) explored the structural effect of a similar roughness strip on the near-wall flow, showing that streaks associated with the quasi-streamwise vortices of the near-wall cycle were suppressed by the roughness, and recovered only some distance downstream of the trailing edge of the roughness strip.

The current study begins to bridge the gap between the statistical picture of Andreopoulos & Wood's (1982) and Pearson *et al.*'s (1997) flow visualizations, by (i) closer examination of the nature and behaviour of the internal layers and their relation to other statistical properties of the flow, which offer the best intuitive

| | $x$ (cm) | $U_\infty$ (m s$^{-1}$) | $\delta$ (mm) | $\theta$ (mm) | $Re_\theta = U\theta/\nu$ | $Re_\tau = u_\tau\delta/\nu$ |
|---|---|---|---|---|---|---|
| Unperturbed | 0.50 (7.4) | 20.16 (20.60) | 17.0 (17.6) | 2.1 (1.9) | 2770 (2560) | 910 (970) |
| | 58.0 (62.4) | 20.09 (20.42) | 24.1 (25.8) | 3.1 (2.9) | 4070 (3870) | 1200 (1320) |
| Perturbed | 0.25 (7.4) | 20.20 (20.65) | 17.2 (18.4) | 2.1 (2.2) | 2770 (2970) | |
| | 58.0 (62.4) | 20.07 (20.50) | 24.4 (26.7) | 3.3 (3.1) | 4330 (4150) | |

TABLE 1. Mean flow properties at streamwise extrema of sampling area for hot wire (PIV).

perspective on how impulsive perturbations affect a turbulent flow; (ii) an examination of the turbulent spectra associated with the downstream flow, to understand how the previous observations about the near-wall cycle manifest themselves energetically; and (iii) an analysis of the distribution of swirling content and discrete vortex cores in the flow field downstream of the perturbation, in order to understand the structural modifications occurring in the flow and how their relaxation relates to the other measures of the return to equilibrium.

## 2. Experimental method

### 2.1. *Facility and apparatus*

The turbulent boundary-layer experiments were performed in the 2 ft $\times$ 2 ft wind tunnel at Caltech over a flat plate, where the ceiling was adjusted to maintain a zero pressure gradient (spatial variation in pressure coefficient $\Delta C_p \ll 0.01$ over the range of streamwise measurement locations). The plate was constructed of optically clear acrylic to allow for proper illumination of particle image velocimetry (PIV), with removable plugs to allow positioning of a hot-wire probe. The boundary layer of the smooth flat plate was tripped 19.0 mm downstream of the tip of the elliptic leading edge by a 0.76 mm diameter cylindrical wire glued to the surface, and the effectiveness of the trip was confirmed by identification of the virtual origin for the turbulent boundary layer, as described below. Downstream of the trip, an insert was fitted into the smooth flat plate allowing for a short patch of two-dimensional roughness elements to protrude above the surface of the plate. This short patch, referred to as the impulse or perturbation, consisted of four bars of two-dimensional, $k$-type roughness, each 1 mm in amplitude, 1.57 mm thick and separated by 6.35 mm, giving a ratio of rod spacing $p$ to roughness height $k$ of $p/k = 7.14$ which is consistent with the work of Leonardi *et al.* (2003) in two-dimensional roughness and should maximize the roughness-type behaviour. It was positioned such that its leading edge (the $S \rightarrow R$ transition) occurred 880 mm downstream of the leading edge trip of the flat plate, or at a Reynolds number based on the free stream velocity, $U_\infty$, of $Re_l = 1.15 \times 10^6$ and $Re_\theta = 2770$ (table 1). The roughness patch extended for 25.3 mm or approximately $1.5\delta$ of the smooth wall boundary layer, well within Andreopoulos's impulsive criterion that the impulse should be less than $10\delta$. A schematic of the experimental setup, along with the relative positions of the different measurement locations, is provided (figure 1). The flow field downstream of the roughness impulse was interrogated by hot-wire anemometry and PIV. The measured velocity signal $\tilde{u}(y,t)$, in the following analysis, is decomposed as $\tilde{u}(y,t) = U(y) + u(y,t)$, where the mean profile is $U(y)$ and the turbulent fluctuation is $u(y,t)$; $\sqrt{u^2(y)}$ is the root-mean-square value of $u(y,t)$; $\sqrt[3]{u^3(y)}$ is the cube root of the third-order moment of $u(y,t)$ (which shares the same sign as the skewness but allows for standard outer scaling for consistency with other results).

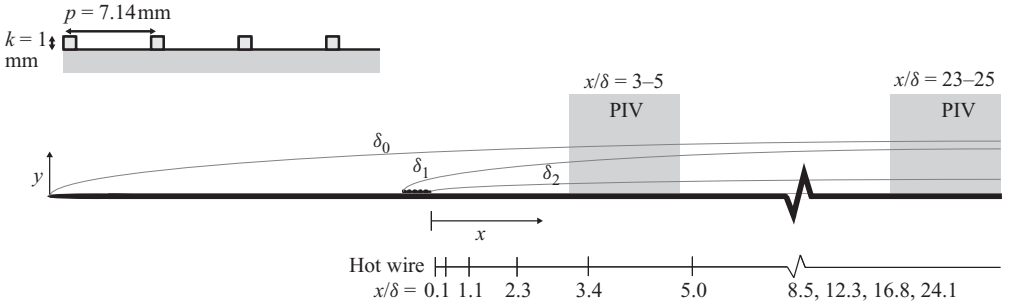


FIGURE 1. A schematic of the arrangement of the flat plate, the roughness strip and the diagnostic locations; not to scale. The internal layers are also marked in order to provide an idea of their relative sizes and development rates.

### 2.2. *Hot-wire anemometry*

For the anemometry, the downstream flow was measured using a 5 μm diameter, $d$, $l = 1.25$ mm active length, platinum-plated tungsten boundary-layer-type probe (Dantec #55$P$05) and an A.A. Labs anemometer (AN-1005), calibrated *in situ* with a fifth-order polynomial fit, against a Pitot probe and Baratron MKS 20 Torr pressure transducer (#220DD). The hot wire had $l/d = 250$ and $l^+ = 67$, where $(l)^+$ indicates scaling on inner units as $l^+ = lu_\tau/\nu$ with friction velocity $u_\tau$ discussed below. According to Hutchins *et al.* (2009), such a large value of $l^+$ at this relatively low $Re_\tau = u_\tau\delta/\nu$ (where the friction velocity $u_\tau = \sqrt{\tau_w/\rho}$ and kinematic viscosity $\nu = \mu/\rho$) can significantly underestimate $\sqrt{u^2(y)}$ near the wall. Using the formulas provided, an underestimate of the peak in $\sqrt{u^2(y)}$ by as much as 30 % is expected, but since the essence of the study is comparative – between perturbed and unperturbed flows – this bias was not considered consequential. The spatial resolution in terms of the Kolmogorov scale, $\eta$, estimated by the local equilibrium approximation (following Morrison *et al.* 2004) was $(2\pi/l)\eta \approx 0.15$.

The hot-wire probe holder was affixed to a vertical traverse (Velmex BiSlide stepping motor, # PXN10-0040-01-71) with 2.5 μm-per-turn precision positioning, which means the uncertainty in the local position was less than $\pm 0.15$ wall units. The traverse was controlled via a script in Labview in order to step through a full velocity profile, after the initial point was set manually, by calibration with a camera. The error in the near-wall positioning was on the order of 100–200 μm, or between 5 and 10 wall units, with a bias towards overestimating the height due to reflections from the flat plate. (By alignment of the unperturbed near-wall peak via comparison with the results of DeGraaff & Eaton 2000, a correction factor for placement error for the initial wall-normal location was prescribed for both perturbed and unperturbed flows). Thus, the nearest wall position measured, using the scaling from the unperturbed case, was approximately 3 wall units.

Data records of $T = 50$ s duration ($TU_\infty/\delta = 6 \times 10^4$) were sampled at $f_s = 60$ kHz ($t^+ = u_\tau^2/f_s\nu \approx 0.73$). Following Hutchins *et al.* (2009), the maximum flow frequency was estimated to be $u_\tau^2/3\nu \approx 13$ kHz, and the frequency response of the anemometer, estimated from the impulse response to be $f_a \approx 15$ kHz (following Freymuth 1977), exceeded this guideline. Velocity time series were recorded at 27 logarithmically spaced wall-normal locations at each of 10 logarithmically spaced streamwise locations. The recording locations ranged from 0.5 cm downstream of the trailing end of the location of the roughness impulse (the $R \to S$ transition), denoted by $x$, to 58 cm downstream,

which corresponds, in terms of the boundary-layer thickness recorded at the most upstream location in the unperturbed case, to a range of 0.3–34 $\delta_0$ downstream, where $\delta_0$ is the boundary-layer thickness of the incoming, unperturbed flow at the location of the perturbation. Spectra were processed using Welch's method on the full time record ($3 \times 10^6$ points), and the local convective velocity was employed in Taylor's hypothesis to express the temporal spectra as a function of streamwise wavenumber, $k_x = 2\pi f/U$ or wavelength $\lambda = 2\pi/k_x$ for comparison with the smooth wall results of Hutchins & Marusic (2007).

### 2.3. *Particle image velocimetry*

The PIV measurements were taken at two streamwise locations centred on 980 mm and 1530 mm downstream of the leading edge ($4\delta_0$ and $35\delta_0$, or $4\delta$ and $23\delta$), which correspond roughly to the streamwise extrema of the hot-wire measurements. The flow field was seeded with an aerosol of bis(2-ethylhexyl)sebacate (DEHS) (0.25 μm modal size, LaVision Aerosol Generator #1108926) and a streamwise–wall-normal plane was illuminated by a double-pulsed Yag laser at 1000 Hz (10 μs between pulses). Images were recorded at resolution $1024 \times 1024$ pixels from a Photron Fastcam APX-RS camera, using a 170 mm Tamron macro lens, such that the physical size of the PIV images was $38 \times 38\ \mathrm{mm}^2$, allowing full coverage of the boundary-layer thickness. Using the scaling from the unperturbed flow, this corresponds to a resolution per vector of $0.017 \times 0.017$ outer units or $16.3 \times 16.3$ inner units. The first two vectors nearest the wall were discarded, due to seeding reliability issues and reflection difficulties in that domain of the flow field, and thus the closest velocity to the wall which is treated as well-resolved is located approximately 50 wall units from the wall. The velocity fields were processed with PIV software from LaVision, using a double-pass approach, with windows of 32 and then 16 pixels at 50 % overlap to produce each velocity vector.

## 3. Results

In what follows, the mean flow properties for the unperturbed flow and the flow perturbed by the static impulse are presented, with validation of the unperturbed case against previous experiments. The behaviour of the roughness impulse is compared to previous impulsively perturbed flows and the internal layers resulting from the perturbation are identified and interpreted. The effect of the perturbation on the turbulence statistics, the spectral energy distribution and the spatial distribution of vortices on the downstream flow are all presented, and a physical interpretation is offered to connect the key features of the perturbed flow and their importance to boundary-layer modification.

### 3.1. *Mean flow properties*

The essential flow properties for both the hot wire and PIV rounds of experiments are summarized in table 1, and some key features of the flow field are described below. The boundary-layer growth of the unperturbed flow indicates a virtual origin for the turbulent boundary layer, based on comparison with Prandtl's quasi-empirical formulation, at approximately 0.22 m downstream of the leading edge trip, and thus 0.66 m upstream of the roughness impulse location (figure 2).

The friction velocity $u_\tau$ for the unperturbed flow was estimated by the Clauser method (3.1) with $\Delta U = 0$ using

$$\frac{U}{u_\tau} = \kappa^{-1} \ln \frac{y u_\tau}{\nu} + C - \frac{\Delta U}{u_\tau} = \kappa^{-1} \ln \frac{y}{z_0} \tag{3.1}$$

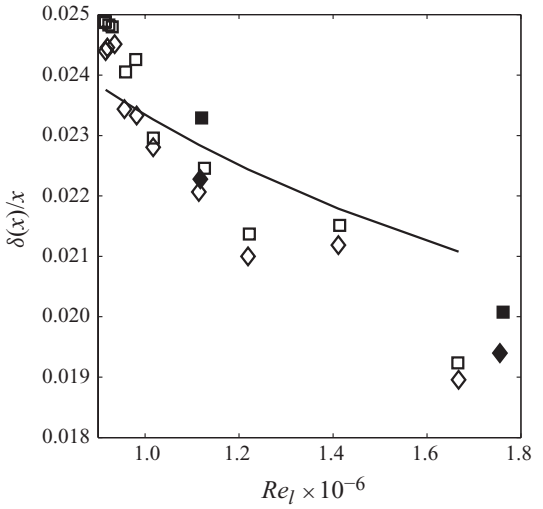


FIGURE 2. The development of the unperturbed and perturbed boundary layers, from the hot wire and from the PIV. The Reynolds number based on downstream distance has been corrected to reflect the approximate location of the virtual origin. For the hot wire: ◇, unperturbed; □, perturbed; and for the PIV: ◆, unperturbed; ■, perturbed; ——, $\delta(x)/x = (Re_x)^{-1/5}$.

and also independently verified by the momentum integral approach; this method was also applied for the perturbed case, employing the roughness function $\Delta U$. However, for the perturbed case, neither method strictly applies, due to the non-equilibrium conditions downstream of the perturbation. Therefore, in addition to these inferential techniques, the friction velocity is also reported directly by linear fit using the no-slip condition and the first velocity measurement nearest the wall (which occurs at $y^+ \approx 3$–7), although here too the result is suspect since the linear profile is not strictly applicable this far out, in addition to the uncertainty in the wall position which can significantly affect the value of the slope of the velocity profile. Using this technique, the perturbed flow is seen to demonstrate a reduction in $C_f$ immediately downstream of the roughness strip, and then an overshoot in the recovery, similar to the report by Pearson *et al.* (1997), and characteristic of the nonlinearity of the perturbation (figure 3). Since each of these techniques suffers from significant sources of uncertainty, scaling throughout the remaining results is accomplished in terms of outer variables or in terms of the inner scales corresponding to the unperturbed case only.

The mean velocity profiles for the unperturbed and perturbed flow were recorded both by hot wire and PIV. The profiles for the unperturbed flow (and turbulence intensity profiles, below) are compared against those reported by DeGraaff & Eaton (2000) for $Re_\theta = 2900$ which corresponds to the fifth or sixth downstream recording position, $Re_\theta = 2850$–$2940$ in figure 4. The mean profiles demonstrate excellent agreement. For the turbulence intensity profile, the degree of the underestimate of the magnitude of the near-wall peak is lower than that predicted by application of the fit in Hutchins *et al.* (2009) for the value of $l^+$ – on the order of 20 % at the peak – but as mentioned above, the discrepancy is not significant to comparisons between perturbed and unperturbed flows. In any case, it would appear that the underestimate can be attributed entirely to the spatial resolution of the probe. The noise floor for the PIV is the error in the peak location of the cross-correlation algorithms, estimated

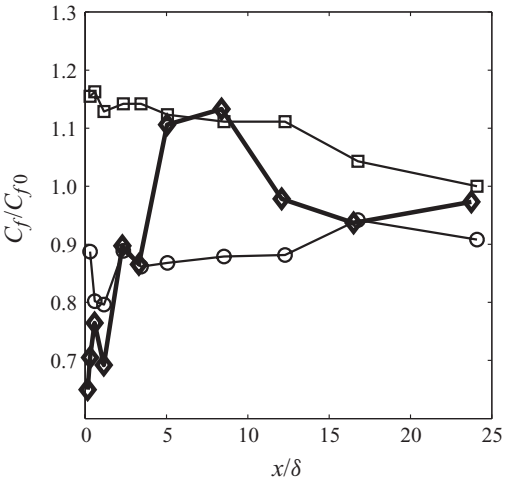


FIGURE 3. The development of the unperturbed and perturbed friction coefficients, from the hot wire. The coefficient derived from the first velocity value measured nearest the wall provides a rather smooth curve, in the unperturbed flow, albeit lower than the value inferred by Clauser's method, and in the perturbed case, the overshoot in the recovery of $C_f$ is observed. ○, unperturbed $2\nu/U\partial U/\partial y(0)$; □, unperturbed Clauser method; ◇, perturbed $2\nu/U\partial U/\partial y(0)$. The overshoot and recovery trends are consistent with those observed in previous studies.

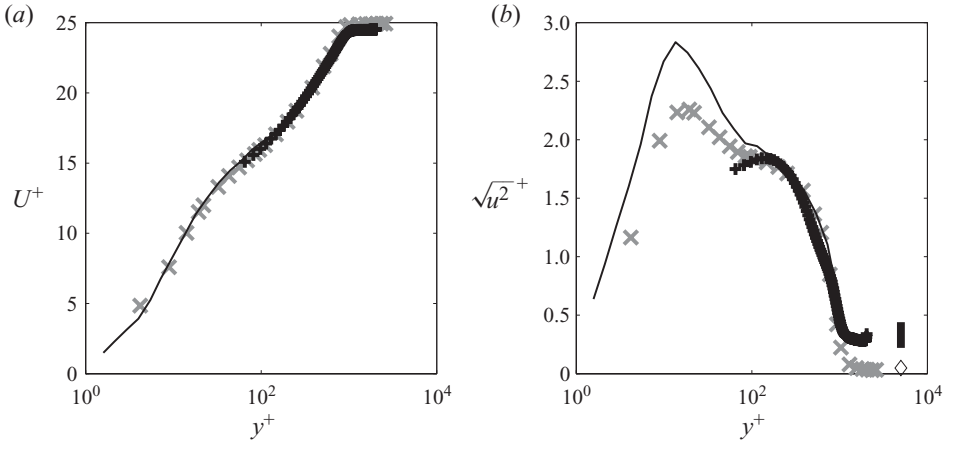


FIGURE 4. (*a*) The mean velocity profile for the unperturbed smooth wall, measured by hot wire and PIV and plotted in wall units against the profile recorded by DeGraaff & Eaton (2000) at similar $Re_\theta$. (*b*) The streamwise turbulence intensity profile for the unperturbed flow, measured by hot wire and PIV and plotted in wall units. ×, hot wire, $Re_\theta = 2940$; +, PIV, $Re_\theta = 2560$, with its estimated noise floor shown as the black bar; —, DeGraaff & Eaton (2000), $Re_\theta = 2900$, with their free-stream turbulence intensity marked by ◇.

by Westerweel (1997) at between 0.05 and 0.1 pixel, which for the current recording translates into a floor of free-stream turbulence intensity of 0.9%–1.8 %, or in the inner units shown below, $u^+_{floor} \approx 0.22$–$0.44$, significantly higher than that of the hot wire.

The mean velocity profiles are compared between the perturbed and unperturbed flows in figure 5. Immediately downstream of the perturbation, there is a significant velocity deficit, particularly for $y/\delta < 0.3$–$0.4$, which corresponds to about six times

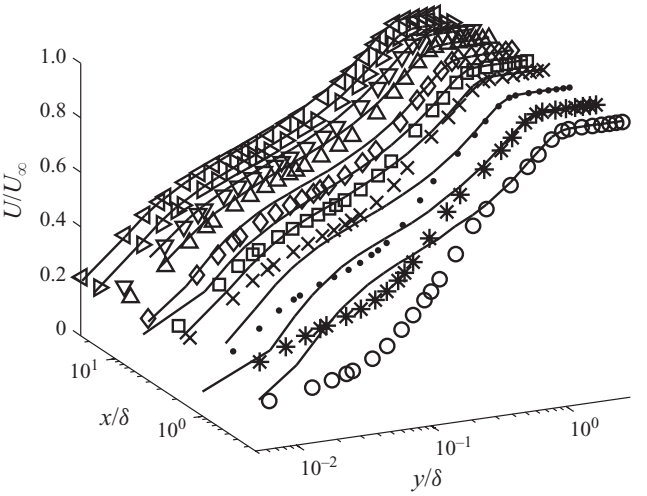


FIGURE 5. The mean velocity profile, in outer units, for the perturbed flow, in symbols. Perturbed: $x/\delta =$ 0.3 ○; 0.6 ∗; 1.1 •; 2.3 ×; 3.3 □; 5.0 ◇; 8.4 △; 12.1 ▽; 16.5 ▷; 23.7 ◁; —— for profiles of the unperturbed flow at corresponding streamwise positions.

the roughness height $k$. This deficit persists until approximately $15\delta$ downstream of the trailing edge of the perturbation. There appears to be a persistent, albeit small, velocity deficit even farther downstream and across the velocity profile, consistent with the results of Andreopoulos & Wood (1982).

By plotting the discrepancy in the mean velocity profiles between the perturbed and unperturbed cases,

$$\Delta\frac{U}{U_\infty}(x, y) = \frac{U}{U_\infty}(x, y)_{perturbed} - \frac{U}{U_\infty}(x, y)_{unperturbed}, \tag{3.2}$$

as a contour map in wall-normal and streamwise directions, the recovery behaviour of the mean velocity profile can be seen quite clearly (figure 6). The 'growth rate' of the peak of the velocity discrepancy can also be plotted as a means of estimating the rate at which the discrepancy moves away from the wall (while simultaneously decreasing in magnitude).

From the mean velocity profiles, the major relaxation of the perturbed flow appears to occur over a distance on the order of $10\delta$, although even then the relaxation is not complete. The noise in the wall shear stress result precludes drawing a conclusion about the rate of its relaxation.

### 3.2. *Internal layers*

The internal layers, marked $\delta_1$ and $\delta_2$ in figure 1, represent the mean extent to which different boundary conditions have influenced the flow. Andreopoulos & Wood (1982), following prior theoretical work, sought to identify the boundaries of the internal layers and measure their growth as a function of the strength of the perturbations due to the roughness patch, a quantity measured by the logarithmic difference between the two roughness heights, $z_{0i}$, associated with each transition, $S \to R$ and $R \to S$; $z_{01}$ represents the incoming, unperturbed flow, $z_{03}$ the flow far downstream of the perturbation and $z_{02}$ the flow over the impulse itself. In order to measure the roughness height, Clauser's formulation (3.1) can be rewritten assuming that the near-wall

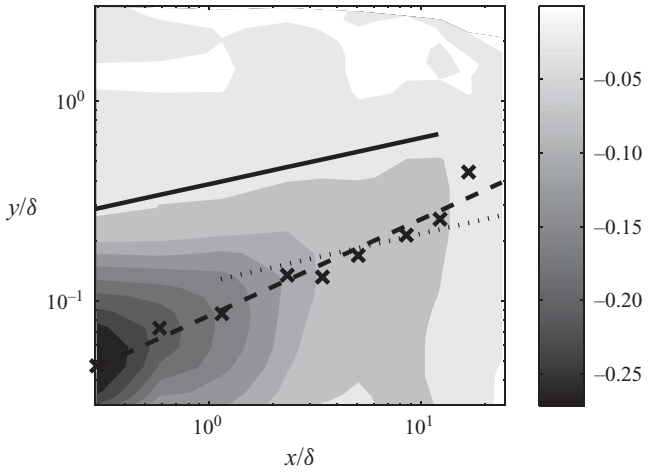


FIGURE 6. The discrepancy in the mean velocity profiles between the perturbed and unperturbed cases is shown in grey contours; the peaks for each streamwise location at which the velocity discrepancy is greatest are marked (×) and a curve is fitted by least squares (- -, $y/\delta = 0.1(x/\delta)^{0.5}$). The approximate intercept for the fit is just below the height of the roughness elements: $0.05y/\delta = 0.83k$. Also, internal-layer best fits, calculated below, are included (——, $\delta_1/\delta = 0.4(x/\delta)^{0.2}$; . . ., $\delta_2/\delta = 0.1(x/\delta)^{0.2}$) for reference.

velocity profile scales on that height as

$$z_0 = \frac{\nu}{u_\tau} \exp[-\kappa\,(C - \Delta U/u_\tau)]. \tag{3.3}$$

It follows that the roughness scale of the incoming flow, $z_{01}$ is simply $z_{01} = (\nu/u_\tau)\exp[-\kappa C] \approx 0.0026\,\text{mm}$ since there is no velocity deficit there. The roughness function $\Delta U/u_\tau$ can then be measured experimentally by simple subtraction of the experimental profile, in the physical region of the logarithmic layer for the unperturbed flow, from the logarithmic fit, using $\kappa = 0.41$ and $C = 4.9$ (following Andreopoulos & Wood 1982 for consistency). Far downstream, $\Delta U/u_\tau \approx 0.31$ and thus $z_{03} \approx 0.0028\,\text{mm}$, for the roughness height downstream of the impulse. Although no data were collected over the elements themselves, using the downstream position nearest to the impulse yields $\Delta U/u_\tau \approx 4.12$ and $z_{02} \approx 0.014\,\text{mm}$. Thus, the strength of the impulse can be estimated by $M_{S\to R} = \ln[z_{01}/z_{02}] \approx -1.7$ and $M_{R\to S} = \ln[z_{02}/z_{03}] \approx 1.6$. Antonia & Luxton (1971*a*) reported $M_{S\to R} = -4.6$ and $M_{R\to S} = 5.8$; Andreopoulos & Wood (1982) reported $M_{S\to R} = -3.67$ and $M_{R\to S} = 4.34$ (although it is worth noting that there appears to be a sign error in their results which, if corrected, would result in $M_{R\to S} = 2.86$). The smooth to rough transition is expected to have a stronger roughness step, since the corresponding velocity deficit should be greater than the velocity deficit once recovery is underway downstream; this expectation is met by both the current results and the corrected results from Andreopoulos & Wood (1982); Antonia & Luxton (1972) do not formally report their rough-to-smooth step strength, but a value for their study is reported by Andreopoulos & Wood (but perhaps with the same sign error?) which is not amenable to simple correction.

The calculations of impulse strength are ultimately unreliable, however, both because of the non-equilibrium nature of the flow, which in principle renders much of this analysis unjustified in a general sense and also in this particular experiment, the logarithmic region of the velocity profile is quite small (only two to four data points)

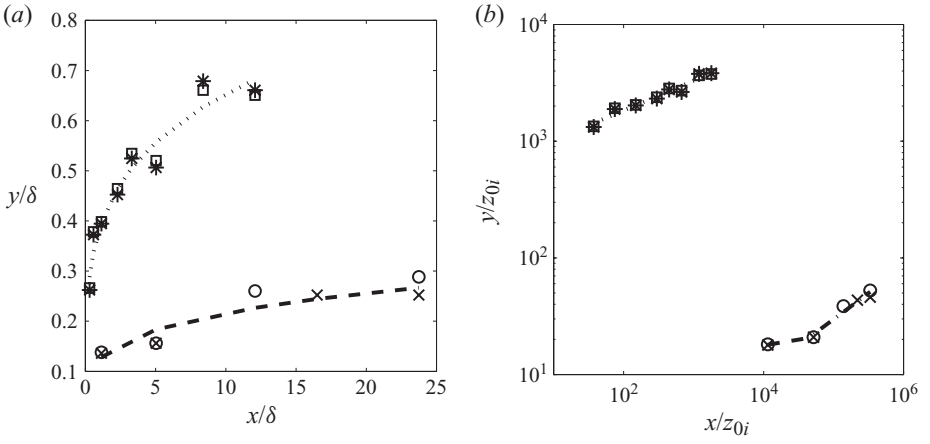


FIGURE 7. The development of the internal layers, calculated by both methods described above. (*a*) Plot and fit in outer units. For $\delta_1$: □, via $y^{1/2}$-scaling; ∗, via $\partial U/\partial x$; for $\delta_2$: ○, via $y^{1/2}$-scaling; ×, via $\partial U/\partial x$; least squares best fits: · · ·, $\delta_1/\delta = 0.4(x/\delta)^{0.2}$; - -, $\delta_2/\delta = 0.1(x/\delta)^{0.2}$. (*b*) Scaled by the appropriate estimated roughness scales, $z_{0i}$. In this case, two distinct slopes are identified for the second internal layer, the first significantly shallower, persists for $x < 5\delta$ at which point the layer begins to grow more quickly (although the first slope is only a pair of points) and is fit by $\delta_2/z_{03} = 7.2(x/z_{03})^{0.1}$; the latter $\delta_2/z_{03} = 0.2(x/z_{03})^{0.5}$; the first internal layer is fit by $\delta_1/z_{02} = 570(x/z_{02})^{0.3}$.

except very far downstream, so there is a significant challenge in fitting both of the open parameters in the log law simultaneously (and for the above analysis, the value of $u_\tau$ was fixed to the smooth wall value, exposing further uncertainty). However, similar trouble beset previous results also, so at least for comparative purposes, these values are instructive in indicating that the steps are comparable between experiments, and also the general trend that the $S \to R$ transition is more abrupt than the $R \to S$ transition indicates that the $R \to S$ non-equilibrium condition should persist farther downstream, in terms of the extent of influence of the perturbation on the flow, since the abrupt transition will equilibrate more quickly.

As described above, the internal layers represent precisely this extent of the influence of the new boundary condition on its neighbouring flow, in the mean sense. There are two methods for ascertaining the location of the internal layer: Andreopoulos & Wood (1982) employed streamwise differentiation of successive mean velocity profiles to identify regions of the profile which indicate the existence of a finite layer by virtue of their streamwise constancy; Antonia & Luxton (1971*b*) proposed, by dimensional argument, that the form of the velocity profile which emphasizes the functional dependence of the velocity gradient on the local wall shear stress must scale the mean velocity profile as $y^{1/2}$. By plotting successive profiles of the mean velocity profile in that scaling, kinks appear in the profile which naturally correspond to the boundaries of different internal layers, and can be identified by visual inspection. Neither of these methods is wholly adequate, due to numerical noise in the differentiation step in the former, and the somewhat subjective identification procedure for 'kinks' in the latter, but both methods tend to converge and thus reinforce a reasonably clear picture of the internal-layer development.

The internal-layer development can be scaled on the corresponding roughness scales developed above or alternatively can be scaled on the standard outer scaling for the boundary layer as a whole (figure 7), where a line is fitted by least squares regression

to a power law model. Previous studies reported using the roughness scaling to identify three distinct regimes for the growth of the internal layers; in the current study, it appears that perhaps two distinct regions can be identified, but not with high confidence.

The internal-layer growth can also be measured dimensionally (without scaling), and it is found that $\delta_1 \sim x^{0.3}$ and $\delta_2 \sim x^{0.1}$, such that the exponent of the dimensional growth rate for the second internal layer is approximately half that of the first internal layer, consistent with the findings of Antonia & Luxton (1971*a*) and Antonia & Luxton (1972), who reported growth rates of $\delta_1 \sim x^{0.7}$ and $\delta_2 \sim x^{0.4}$.

It is worth noting that for the outer-scaled internal-layer growth, Pearson *et al.* (1997) also observed roughly the same exponents for the two internal-layer boundaries, $\delta_1/\delta \sim (x/\delta)^{0.15}$ and $\delta_2/\delta \sim (x/\delta)^{0.17}$. So, although the scaling on roughness height does not appear to produce the trends previously reported, the outer scaling appears to collapse both internal layers to the same power such that they are distinguished only by a multiplicative constant, suggesting that the traditional outer scaling is not only more reliably measured, but potentially more instructive.

The second internal layer (representing the $R \rightarrow S$ transition) does not appear to approach the edge of the boundary layer at all; rather it persists at an intermediate height, near the edge of the inner layer, for all of the streamwise recording positions. This behaviour is consistent with the observation above that the $R \rightarrow S$ transition is less abrupt, along with the findings of previous experimenters.

The least squares fit for the evolution of the first internal layer, which represents the abrupt $S \rightarrow R$ transition, can be plotted to overlay the velocity discrepancy contour map (figure 6) where it appears to trace out the far edge of the velocity deficit. This coincidence is expected, since the first internal layer represents the introduction of the velocity deficit into the flow field via the blockage effect of the first two-dimensional roughness elements on the incoming flow. The reduction of the blockage, at the $R \rightarrow S$ transition, does not manifest itself in the mean velocity discrepancy map due to its lack of abruptness.

### 3.3. *Turbulence statistics*

Turbulence statistics were calculated in the streamwise direction from the hot wire, along with some measurements from the PIV for validation (although the wall-normal range of the PIV was insufficient to reach the near-wall peak and was primarily aimed at the region of flow at or above the height of the roughness elements themselves). The hot wire results tend to underestimate the turbulence intensity for $y^+ < 200$ which is approximately the edge of the inner layer, compared with the results of DeGraaff & Eaton (2000) in figure 4, as expected based on the high value of $l^+$. The PIV suffered a similar drop in turbulence intensity as it approached the inner layer, likely due to smoothing over the intense gradients in this near-wall region. However, as mentioned above, the remainder of the study is purely comparative between the unperturbed base flow and the perturbed flow field, so the underestimate of the near-wall peak should not be significant.

Successive profiles of the streamwise turbulence intensity show a large 'hump' in the profile, which, in uniformly rough walls, is usually associated with differences in near-wall transport due to the influence of the roughness. The 'hump' is centred at $y = 0.08\delta = 1.3k$ immediately downstream of the roughness but evolves throughout the downstream flow field. As with the velocity discrepancy contours, the discrepancy in the streamwise turbulence intensity profiles between the perturbed and unperturbed

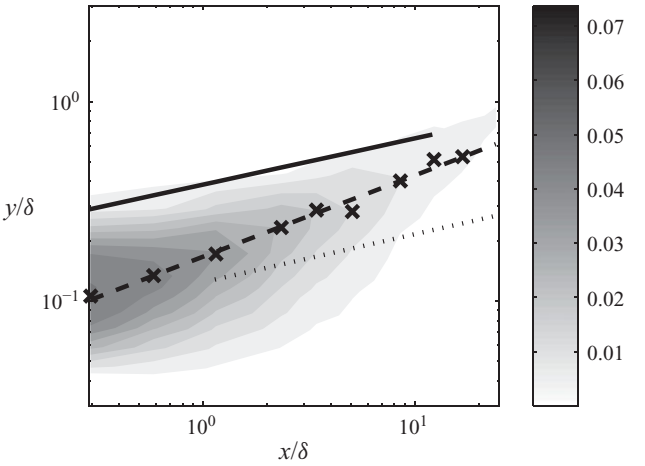


FIGURE 8. The discrepancy in the streamwise turbulence intensity profiles between the perturbed and unperturbed cases is shown in grey contours; the peaks for each streamwise location at which the discrepancy is greatest are marked ($\times$) and a curve is fitted by least squares (---, $y/\delta = 0.2(x/\delta)^{0.4}$). Unlike the mean profile map (figure 6), the approximate intercept for the fit is above the height of the roughness elements: $0.10\delta = 1.67k$. And again, the internal layer boundary best fits, calculated above, are included for comparison.

cases

$$\Delta\frac{\sqrt{u^2(y)}}{U_\infty}(x,\,y) = \frac{\sqrt{u^2(y)}}{U_\infty}(x,\,y)_{perturbed} - \frac{\sqrt{u^2(y)}}{U_\infty}(x,\,y)_{unperturbed}, \tag{3.4}$$

can be viewed as a contour map in wall-normal and streamwise directions in order to visualize the recovery behaviour of the flow field (figure 8).

In this case, the peaks correspond to the 'hump' visible in the individual profiles; however, the contour plot makes clear that this 'hump' moves away from the wall as it decreases in magnitude, and the rate of that progression is faster than the growth rate of either of the two internal layers, meaning that the internal layers represent a quantity which is not linearly related to the transport processes due to the roughness surface condition. Indeed, the fact that the maxima of the 'hump' reside outside the second internal layer, $\delta_2$, was already identified by Andreopoulos & Wood (1982) as signifying that the flow is not merely a linear superposition of individual $S \to R$ and $R \to S$ transitions, in which case the peaks in second-order statistics would occur at $y = \delta_2$.

The successive profiles of the third-order streamwise moment of $u(y, t)$, also show a positive bulge at roughly the height of the roughness elements, along with a corresponding negative bulge at $y = 0.16\delta = 2.7k$. Plotting the discrepancy map again (figure 9) shows that the negative bulge roughly coincides with the region between the two internal layers – the region which was directly influenced by contact with the roughness strip. Overlaying the peak of $\sqrt{u^2(y)}$ from figure 8, however, shows that this peak value tracks the sign change in the third-order moment – and is thus outside of the edge of the second internal layer – as implied by the observation of Andreopoulos & Wood (1982) that the advection and mean wall normal velocity, $V$, are both zero in this region. Using the third-order moment discrepancy plot is thus only a rough indicator of the location of the internal layers, but the physical intuition provided is likely still to be useful. Since the third-order moment can be interpreted as expressing a flux of streamwise kinetic energy (writing $\overline{u^3} \sim \overline{uu^2}$), the

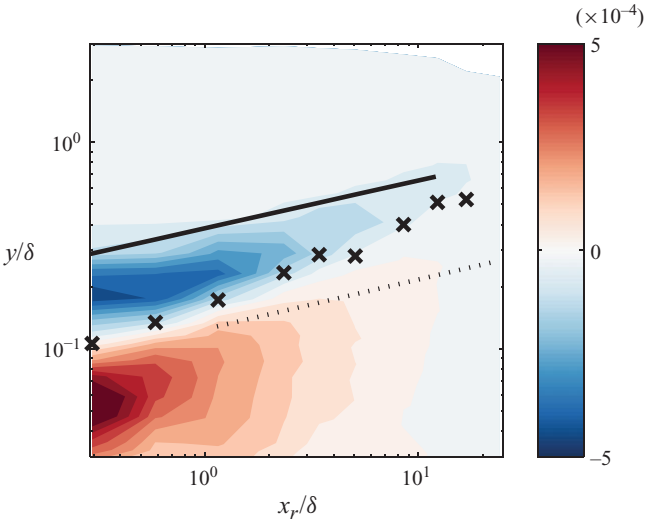


FIGURE 9. The discrepancy in the streamwise third-order moment profiles between the perturbed and unperturbed cases, in red (+) and (−) blue contours. The least squares fits of the internal-layer boundaries are shown: ···, $\delta_2/\delta = 0.1(x/\delta)^{0.2}$; ——, $\delta_1/\delta = 0.4(x/\delta)^{0.2}$. Also shown are the locations of maximum discrepancies in streamwise turbulence intensity (×) from figure 8.

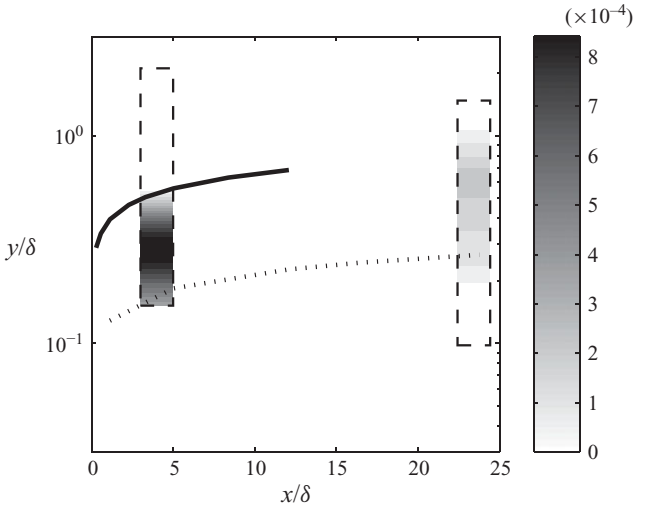


FIGURE 10. The discrepancy in the streamwise Reynolds stress profiles, $-\overline{uv}(y)/U_\infty^2$, between the perturbed and unperturbed cases, from the two PIV measurement locations. The least squares fits of the internal-layer boundaries are shown: ···, $\delta_2/\delta = 0.1(x/\delta)^{0.2}$; ——, $\delta_1/\delta = 0.4(x/\delta)^{0.2}$. Note that the deficit in Reynolds stress corresponds closely to the region between the two layer edges.

negative bulge then represents deceleration between the boundaries of the internal layers, and it captures this region much more precisely than merely the deficit in the mean velocity profile itself. From the PIV measurements, discrepancy maps for the Reynolds stress at two streamwise locations were measured (figure 10); consistent with Andreopoulos & Wood (1982), they indicate that the internal layers also manifest

themselves clearly in mixed moments. However, as should be clear from the above analysis, these moments are not necessary for characterizing to a significant degree the development of the internal layers, and both the PIV and cross-wires present a significant disadvantage when characterizing the near-wall cycle.

Andreopoulos & Wood (1982) observed similar trends, although in a region farther from the wall. They noted that the hump observed in the turbulence intensity plots recalls similar behaviour in the experiments of Smits *et al.* (1979), wherein a flow was perturbed by an impulse of curvature in the form of an abrupt concave or convex bend in an otherwise flat flow field. For the concave bend, the shear stress was observed to increase significantly in the short distance of the curvature impulse, and the peak of this increased shear propagated outwards as a 'stress bore'. Similarly, a bore in the turbulence intensity was observed to propagate outwards, and it was noted that this evolution of the bore was a consequence of both turbulent transport and interactions between the mean shear and local processes. Considering the possibility that the bore dynamics are biased towards influence from the mean shear throughout the boundary layer, then the observed 'hump' in the turbulence intensity plots, which varies with streamwise position downstream of the perturbation, should be scalable by a quantity related to the mean velocity gradient, $u_s$, which represents the continued influence of the near-wall perturbation even farther from the wall:

$$u_s = \sqrt{\left(U_\infty \delta \frac{\partial U}{\partial y}\right)}. \tag{3.5}$$

Under this scaling (figure 11) the 'hump' of $\sqrt{u^2(y)}$ does collapse at all streamwise locations. This collapse indicates that the 'hump' observed in the present study can be considered as a manifestation of the 'stress bore' in the sense outlined in Smits *et al.* (1979). By applying the discrepancy map approach to this mean velocity gradient scaling, $u_s$, the physical region occupied by the stress bore can be identified visually:

$$\Delta\left(U_\infty \delta \frac{\partial U}{\partial y}\right)^{1/2} = \left(U_\infty \delta \frac{\partial U}{\partial y}\right)^{1/2}_{perturbed} - \left(U_\infty \delta \frac{\partial U}{\partial y}\right)^{1/2}_{unperturbed}. \tag{3.6}$$

The discrepancy map (figure 12) immediately shows that, in a rough sense, the stress bore is identical to the region between the boundaries of the two internal layers. Thus, both the deceleration bulge of the third-order moment $\sqrt[3]{u^3(y)}$ and the surplus bulge in $u_s$ provide two physically motivated and robust ways of locating the boundaries of the internal layers, and thereby identifying the region of downstream flow under the influence of an impulsive perturbation. In particular, the fact that the positive bulge in the discrepancy map for $u_s$ neatly demarcates the region between the edges of the two internal layers shows that the 'stress bore' analogy is powerfully descriptive – there is, indeed, an identifiable and persistent 'bore' of shear stress implanted in the downstream flow by the impulsive perturbation.

From a different perspective, roughness is understood to affect the local scale sizes in a flow, so another approach to identifying regions of the flow field influenced by the roughness impulse is to look for regions in which scale sizes vary from the corresponding smooth wall flow. The integral time scale, which is a scale characteristic of the largest scales in the flow, can be defined by the autocorrelation of the velocity time signal, and can be transformed via Taylor's hypothesis into a length scale;

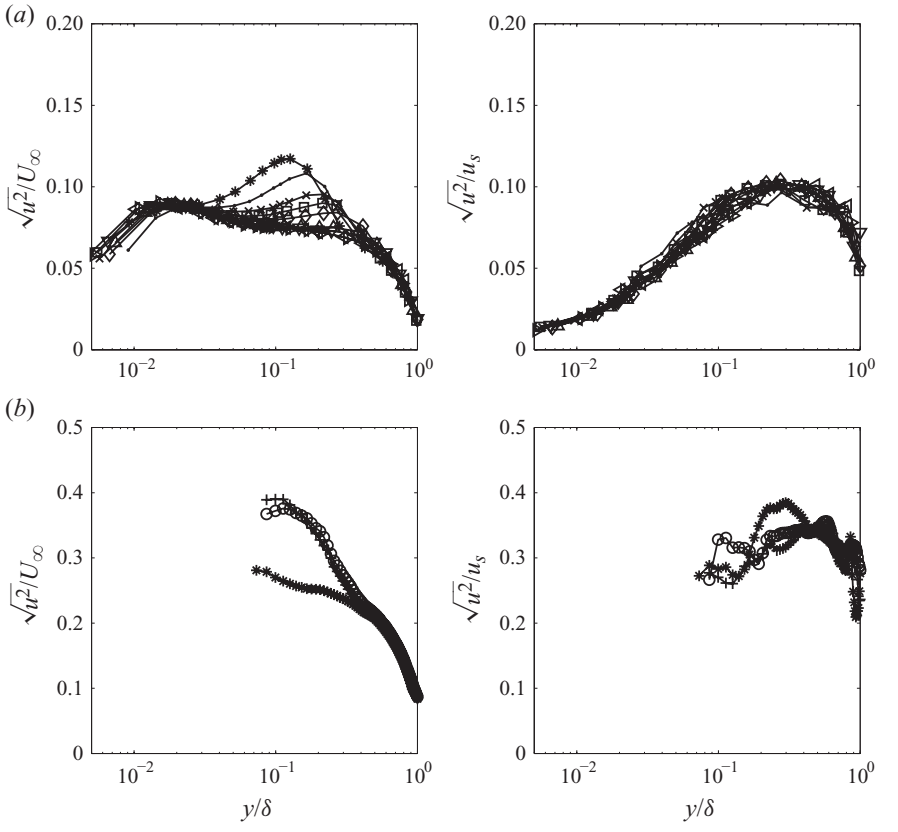


FIGURE 11. (*a*) The turbulence intensity for the perturbed flow under (left) standard outer scaling; and (right) under a velocity scaling based on the mean velocity gradient. Symbols follow figure 5. Note the collapse in the near-wall region, $y/\delta < 0.2$. (*b*) The results from Andreopoulos & Wood (1982) – the collapse is not as clean because of significant scatter in the $\sqrt{u^2(y)}$ data and an insufficient number of streamwise locations.

alternatively, it can be calculated from the streamwise energy spectrum

$$\Lambda_L(x, y) = U(y) \int_0^\infty R_{11}(x, y, t)\, \mathrm{d}t = \frac{2}{\pi} \lim_{k_x \to 0} \phi_x(k_x). \tag{3.7}$$

The integral scale at each wall-normal and streamwise location reveals the relative distribution of the largest scales in the flow field, under the unperturbed and perturbed boundary conditions. The wall-normal distribution in the unperturbed flow has a maximum around $y/\delta \approx 0.1$ with a rapid decay ($\Lambda_L \to 0$) at the wall and a slow decay ($\Lambda_L \to 0.4\delta$) towards the edge of the boundary layer. The integral scales increase about 15 % on average over the streamwise extent of the plate. The perturbed flow field shows a disruption of this distribution, as the size of the largest scales is depressed near the perturbation. A map of the ratio of these two sets of integral scales (figure 13) indicates that the integral scale in the perturbed case is as little as half the size of the unperturbed flow, in the immediate vicinity of the perturbation. However, in the region of flow between the mean boundaries of the two internal layers, there appears to be an increase in the size of the integral scales – this increase is even more prominent when the length scale is calculated by the spectral method. Antonia & Luxton (1971*a*)

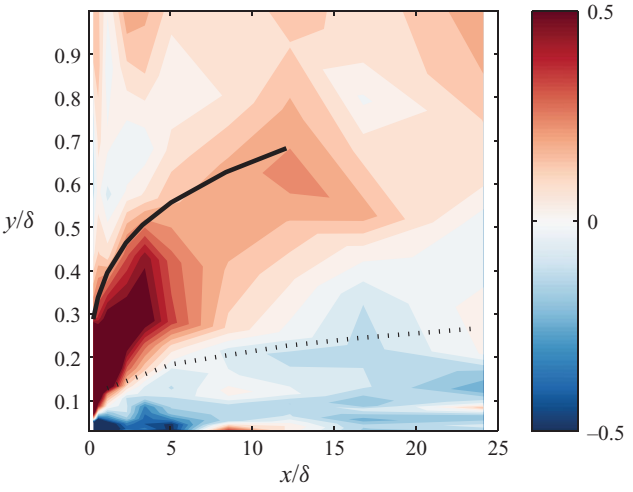


FIGURE 12. The discrepancy in the mean velocity gradient scale $u_s$ between the unperturbed and perturbed flows (3.6) overlayed with the best fits of the two internal-layer boundaries – symbols from figure 9. In this case, note that the surplus in shear stress corresponds precisely to the region between the boundaries of the two internal layers.

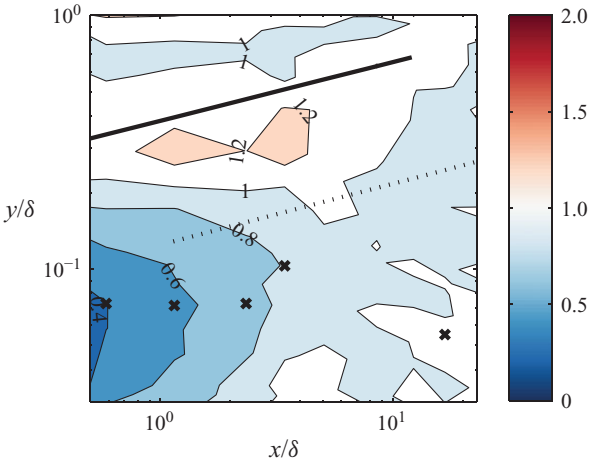


FIGURE 13. The ratio of the map of integral scales for the perturbed flow to the smooth flow, $\Lambda_L/\Lambda_{L_0}$ overlayed with the best fits for the two internal-layer boundaries as in figure 9 and also $\times$ for extrema (among wall-normal positions) at each streamwise location.

reported that integral length scales were significantly suppressed downstream of the $S \rightarrow R$ transition, but inflated downstream of the $R \rightarrow S$ transition, with the change occurring near the boundary of the internal layer in each case. However, their cases dealt with the transition from one equilibrium condition to another; for the impulsive disturbance, the $R \rightarrow S$ transition should be only partial, since the rough condition was never fully established. Therefore, the region of increase in the integral scales between the boundaries of the two internal layers reflects the displacement of larger scales from near the wall to the outer flow, at the $S \rightarrow R$ transition; then, the smaller scales which began to develop over the roughness persist within the second internal

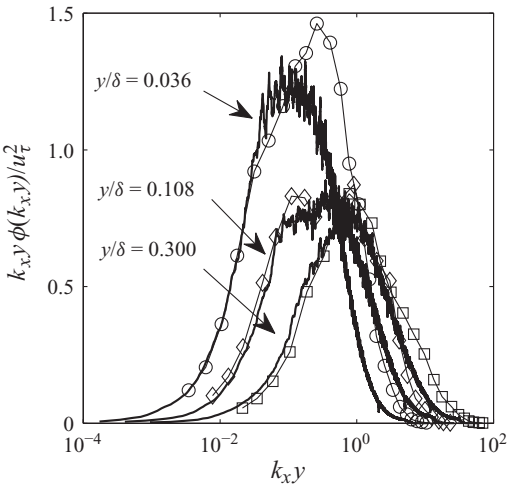


FIGURE 14. The pre-multiplied spectra of the smooth wall, in terms of streamwise wavenumber and wall-normal location. The current data, at the streamwise location corresponding to $Re_\theta = 2840$, —, at the wall-normal locations marked. For comparison, the results of Erm & Joubert (1991) at $Re_\theta = 2810$: ○, $y/\delta = 0.04$; ◇, $y/\delta = 0.10$; □, $y/\delta = 0.35$. As noted above, the turbulence intensity near the wall tends to be underestimated, and that carries over in this context, where the energy in the small scales also tends to be suppressed slightly.

layer, while the integral scales regrow, yielding the significant decrease in length scales observed downstream near the wall.

### 3.4. *Composite spectra*

The individual temporal spectra from the time series were transformed by Taylor's hypothesis into spatial spectra in streamwise wavenumber, $k_x$. For the unperturbed case, these spectra were compared at a similar Reynolds number to the results of Erm & Joubert (1991) for validation (figure 14). Although there were some discrepancies in the validation, consistent with the underestimate in turbulence intensity near the wall reported above, the overall comparative analysis between perturbed and unperturbed flows remains unaffected. And as noted above, the friction velocity used in all the normalizations corresponds to the incoming unperturbed flow.

Composite pre-multiplied spectra can be assembled from contours of the individual $1D$ spectra when arranged in wall-normal sequence. This procedure, explained in detail in Hutchins & Marusic (2007), provides a physical sense of the distribution of spectral energy when the composite spectra are viewed in logarithmic coordinates since equal energetic contributions appear as equal contour areas of the composite spectra at a given wall-normal distance. Considering first the smooth wall composite spectra, at the beginning and end of the test section (to view the maximum spread of $Re_\theta = 2770$–$4070$) allows identification of a few key features (figure 15), including the inner peak $\lambda_x^+ \approx 1000$, $y^+ \approx 25$ and the peak for very large-scale motions (VLSM) at $\lambda_x/\delta \approx 6$ as well as the large-scale motion (LSM) peak, common to all boundary layer flows, at $\lambda_x/\delta \approx 3$ described in detail in Monty *et al.* (2009). The LSM peak at $\lambda_x/\delta \approx 3$ is quite prominent at both flow points, while the larger VLSM peak at $\lambda_x/\delta \approx 6$ only begins to appear at the furthest downstream position (and even then its presence is subtle). The near-wall peak is quite distinct across a broad range of wavelengths; its location farther from the wall than other investigators found is a consequence of measurement error of the wall-normal location.

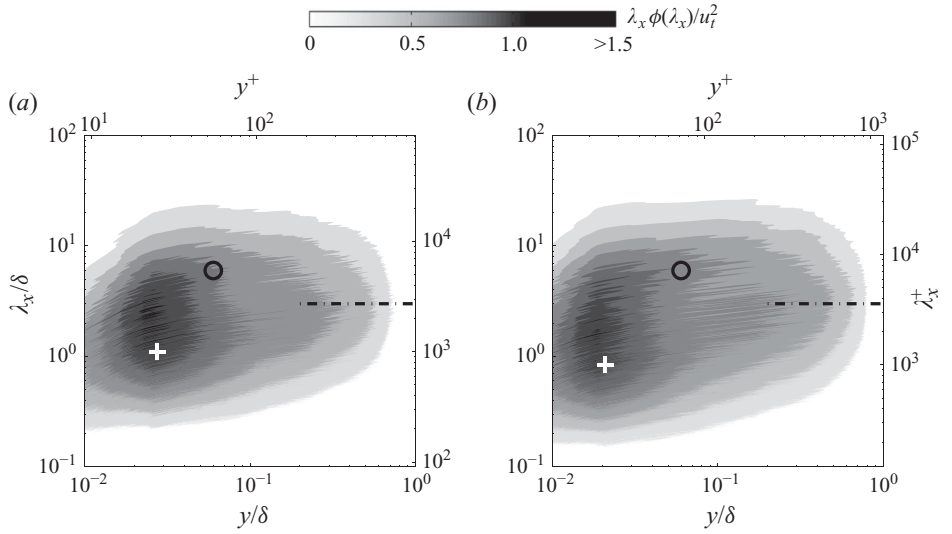


FIGURE 15. Composite spectra for the unperturbed case: (*a*) $Re_\theta = 2770$, the white '+' marks the vicinity of the inner peak ($\lambda_x^+ \approx 1000$, $y^+ \approx 25$), the black ○ marks the expected location of the VLSM peak at ($\lambda_x/\delta \approx 6$), and $-\cdot-$ marks the LSM peak along $\lambda_x/\delta \approx 3$; (*b*) $Re_\theta = 4040$ with markings as in (*a*).

The composite spectra are produced for the perturbed flow at all of the downstream measurement locations in figures 16(*a*) and 17(*a*). Although the first few streamwise locations are situated in the immediate vicinity of the recirculation bubble downstream of the last roughness element, and thus the hot-wire signals are not reliable, the abrupt change in the shape of the $\sqrt{u^2(y)}$ profile which occurs between $x/\delta = 0.1$ and $x/\delta = 0.6$ indicates that $x = 1.1\delta = 18.3k$ is well outside of the mean recirculation region. Yet, at this location, there is still an unambiguous suppression of the near-wall peak, particularly at the higher wavelengths. This reduction in the energy of specifically larger scales is consistent with the decrease in the integral scale $\Lambda_L$, representing the largest significant scales in the flow, which was found in the immediate vicinity of the impulse. The recovery of the near-wall peak occurs much more quickly than the dissipation of the displaced spectral energy – located in the region of the 'hump' in the $\sqrt{u^2(y)}$ profiles – implying that the time scale for the generation (or regeneration) of the near-wall cycle is significantly smaller than dissipative time scales in the flow. In addition, the dissipation of the displaced spectral energy is not uniform across wavelength space, rather the higher wavelengths dissipate first, leaving a strong residual concentration of spectral energy around $\lambda_x/\delta \approx 1$–2, which then eventually dissipates far downstream, leaving only the natural LSM peak at $\lambda_x/\delta \approx 3$. This residual displaced energy can therefore be considered as an artificial enhancement to the natural LSM for boundary layers. In figures 16(*b*) and 17(*b*), discrepancy plots of the composite spectra were formed, as was done for the statistical quantities above, but with the additional subtlety that the wavelength spectra between the perturbed and unperturbed flows varied as a consequence of the use of Taylor's hypothesis, and thus for comparison the unperturbed composite spectrum was regridded (by cubic interpolation) to the range of the perturbed spectrum, prior to the subtraction. The unperturbed composite spectra were reasonably robust in the streamwise direction thus making this sort of subtraction justifiable, at least for qualitative observations.

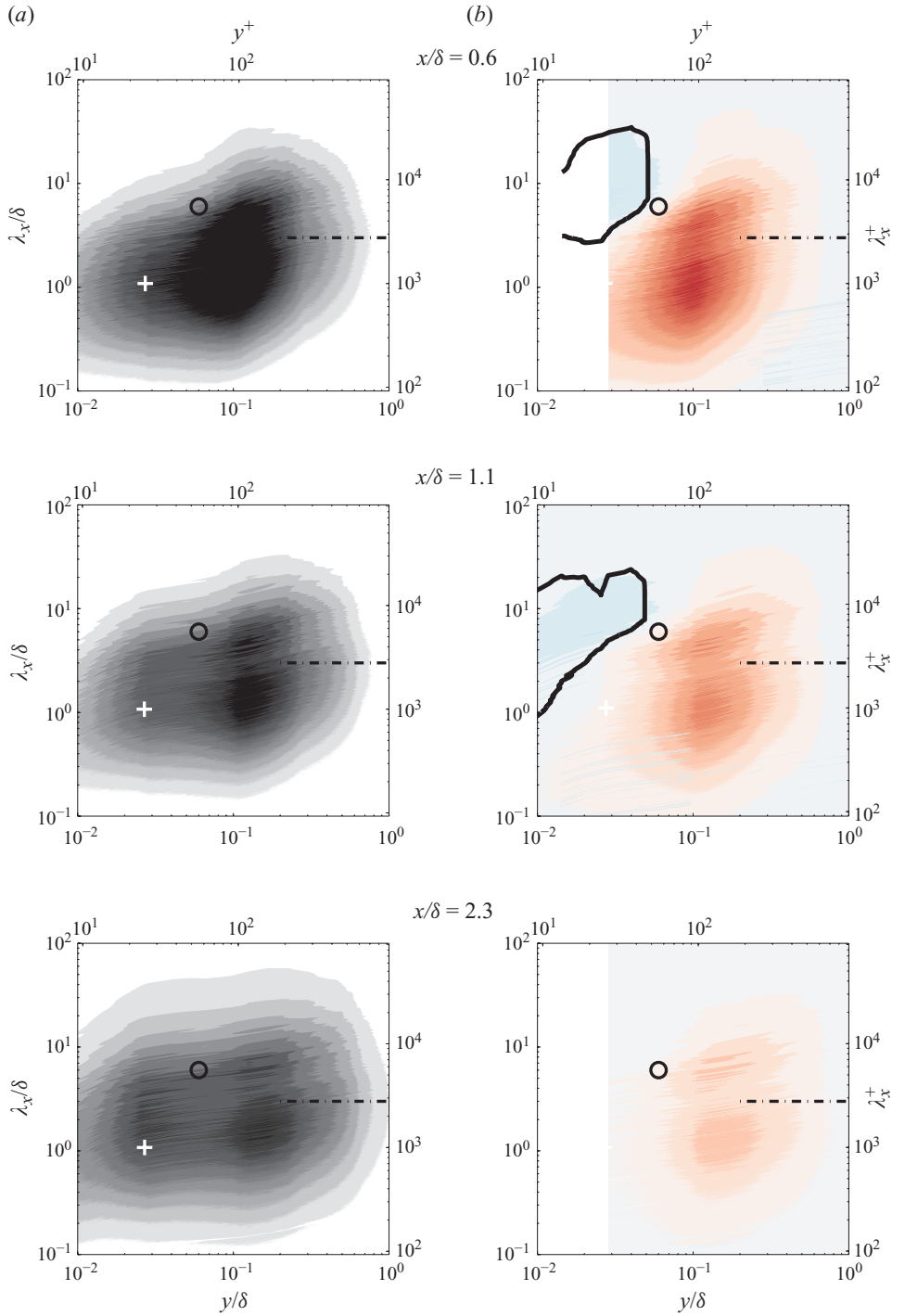


FIGURE 16. (Colour online available at journals.cambridge.org/FLM) (*a*) Composite spectra for the perturbed case: the first streamwise location, $x = 0.1\delta = 1.65k$, is suspected to be within the mean recirculation bubble downstream of the last roughness element; therefore, the third streamwise location $x = 0.6\delta = 10k$, which appears to be downstream of the recirculation region, is shown first. (*b*) The discrepancy maps for the composite spectra, with a range identical to the spectra themselves, but mirrored for negative values (red are positive; blue are negative and are outlined by the contour line which represents a region of spectral content suppressed more than 5 % below the unperturbed flow).

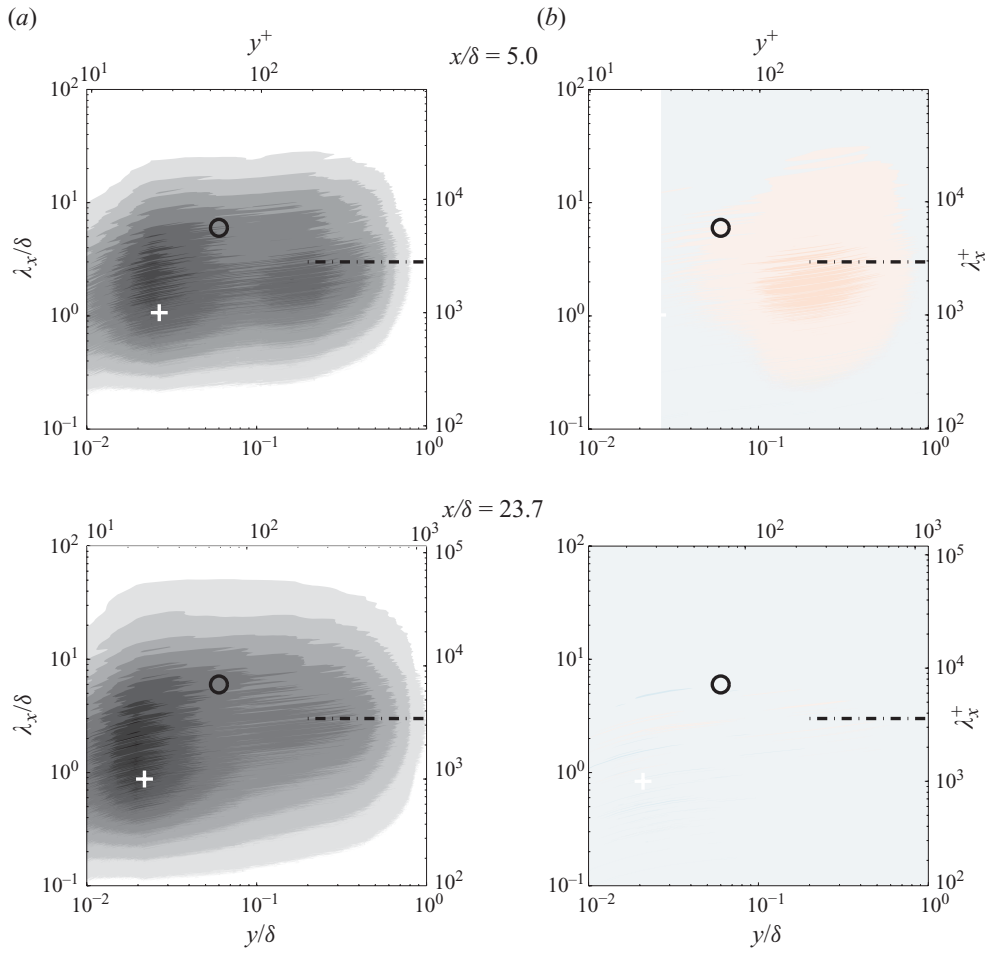


FIGURE 17. (Colour online) (*a*) Composite spectra continued from figure 16 at additional downstream positions. (*b*) Continuation of the discrepancy maps for the composite spectra.

These composite spectra discrepancy maps show clearly the suppression of the near-wall cycle and the displacement of that energy away from the wall.

The interruption of the near-wall cycle, with its quasi-streamwise vortices, was observed directly by Pearson *et al.* (1997) who were able to visualize the flow over the roughness strip itself. They reported a recovery of the 'mushroom-like structures' characteristic of the quasi-streamwise vortices about $x \approx 0.15\delta \approx 5k$ downstream of the trailing edge of the roughness strip, which is somewhere downstream of any recirculation behind sandpaper-type roughness. Similarly, from the spectral maps above, it appears that the near-wall cycle does not begin to recover until well past the reattachment point for the two-dimensional roughness, indicating a minimum regeneration time for the cycle.

### 3.5. *Swirling and vortex structure*

Employing both velocity components in the wall-normal streamwise plane, from the PIV measurements, allows construction of the instantaneous swirling strength field, which provides a physical sense of the amount of swirling motion in the flow field (where swirling strength is defined using the magnitude of the imaginary eigenvalue

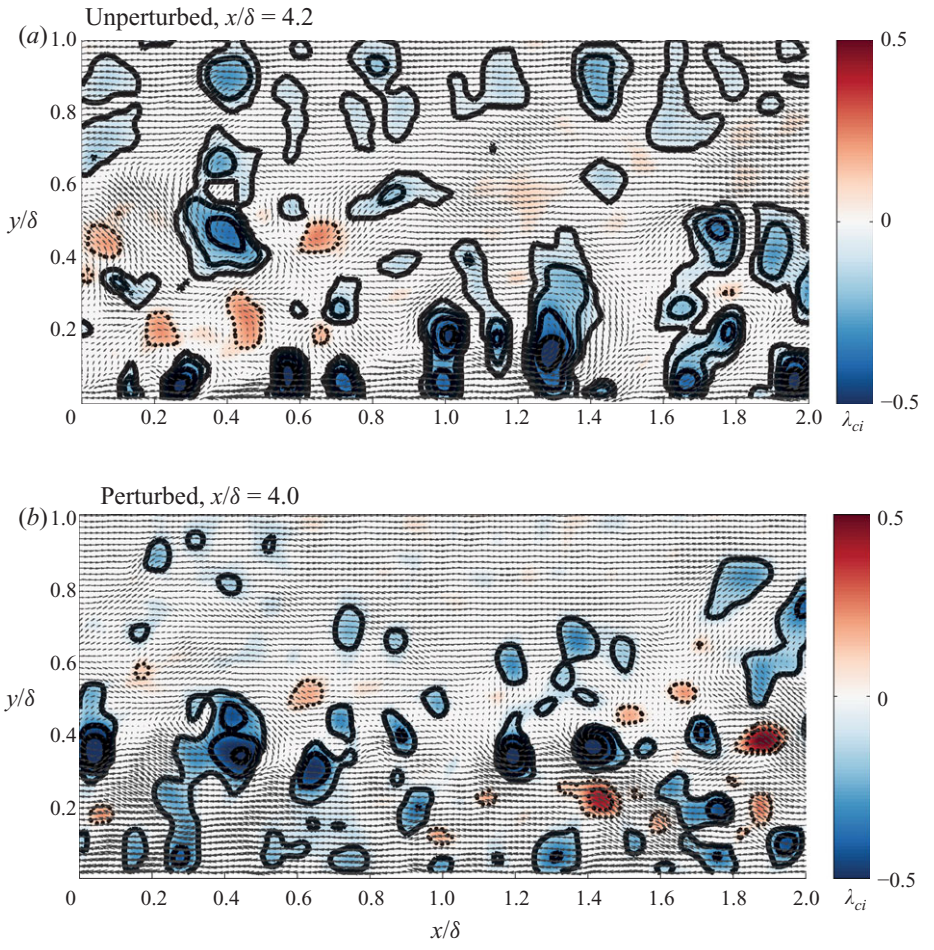


FIGURE 18. (Colour online) The velocity field quivers from the PIV under a Galilean decomposition, where $0.8U$ has been subtracted off; the levels correspond to the swirl, calculated by the same decomposition; prograde in blue (solid lines), retrograde in red (dotted lines). (*a*) Unperturbed, (*b*) perturbed.

from the local velocity gradient tensor, $|\boldsymbol{\lambda}_{ci}|$, following Zhou *et al.* 1999). The naturally unsigned swirling strength can be assigned a directional sense by means of the local sign of the spanwise vorticity field. Negative swirl is referred to as prograde since it is consistent with the rotational sense of the mean shear; positive swirl is referred to as retrograde, following Wu & Christensen (2006).

Two representative frames taken from the PIV results illuminate some of the differences in instantaneous swirl distribution (figure 18). In particular, an increase in the population of prograde vortex cores farther from the wall, in the vicinity of $y/\delta = 0.2$–$0.3$ is readily apparent, as is a decrease in prograde cores very near the wall, although the bias of prograde against retrograde is a topic of ongoing investigation.

The swirling strength field can be averaged over time to produce a profile of the total swirling strength as a function of wall-normal distance (figure 19*a*). The perturbation appears to contribute to an increase in overall swirling at around $y/\delta = 0.2$–$0.3$ at $x/\delta \approx 4$, with a bias towards the increase in prograde swirl. The integrals of the prograde and retrograde swirling profiles are calculated across the boundary layer

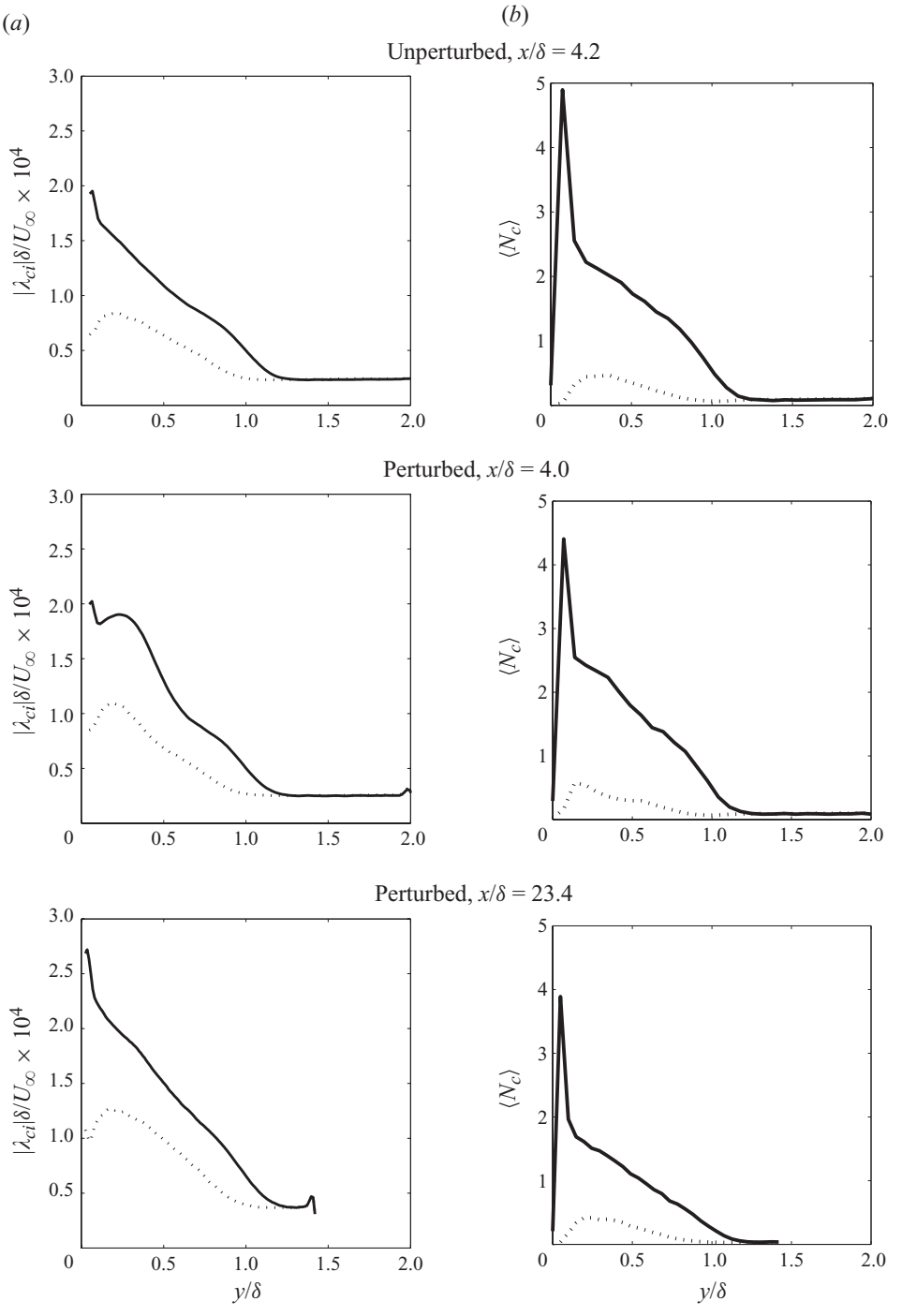


FIGURE 19. (*a*) The profile of swirling strength, averaged in the streamwise direction across the PIV recording window in outer scaling; (*b*) the mean number of distinct vortex cores, per PIV frame, as a function of wall location. ——, prograde; . . ., retrograde.

| | Prograde Swirl | Retrograde Swirl | Prograde Cores | Retrograde Cores |
|---|---|---|---|---|
| Unperturbed, $x/\delta = 4.2$ | 1.00 | 0.61 | 1.00 | 0.18 |
| Perturbed, $x/\delta = 4.0$ | 1.00 | 0.60 | 1.03 | 0.19 |
| Perturbed, $x/\delta = 23.4$ | 1.02 | 0.63 | 0.91 | 0.17 |

TABLE 2. Integrated swirl profiles.

and then normalized by the prograde integral for the upstream unperturbed flow (table 2, leftmost columns). The relatively constant values of the integrated swirl profiles suggest that total swirling is roughly conserved; any generation over the roughness elements, if it occurs, is presumably balanced by the disruption of the near-wall cycle, and the incoming swirling content is merely displaced and reorganized by the roughness impulse.

By using a thresholding criterion based on the mean swirl and the minimum resolvable vortex size, individual vortex cores were identified and counted in order to construct a parallel series of plots, where instead of total swirling strength, the average number of vortex cores per frame of the PIV viewing field, $\langle N_c \rangle$, as a function of wall-normal distance is measured (figure 19*b*). The distribution of discrete cores shows a similar rise in core counts farther from the wall.

As with the aggregate swirl, the integrals of the prograde and retrograde mean core count profiles are calculated across the boundary layer and then normalized by the prograde integral for the upstream unperturbed flow (table 2, rightmost columns). The number of cores, like the aggregate swirl, remains roughly constant, again indicating the redistributive influence of the impulse. Both the aggregate and discrete distributions tend to relax back to the shape of the unperturbed distribution (although not the integral) by the far downstream PIV measurement station.

## 4. Discussion and conclusions

The impulsive roughness perturbation influenced the entire downstream flow field, as far as could be measured, and the extent of the influence was seen to correspond to the growth of two internal layers, as identified in previous work. These internal layers, which previously had been identified from the mean velocity profile were shown to correspond to both a deceleration of the streamwise energy flux, measured via the streamwise third-order moment, and to a change in the mean velocity gradient – both quantities which are easily obtainable from just a single velocity component, and importantly, can be obtained by simple subtraction, without the noisy streamwise differentiation employed in previous investigations. These methods provide a means of measuring the extent of the influence of the impulse, which was shown to generate a stress bore in the flow. The manifestation of this stress bore in the streamwise turbulence intensity was shown to be scaled by a velocity scale based on the mean velocity gradient, indicating that the stress bore itself is, in some sense, disconnected from the boundary condition, and dependent on purely local flow conditions. The immediate consequence of this is the long streamwise persistence of the bore that has been observed by a number of previous experimenters.

The structural observations of Pearson *et al.* (1997) about the suppression of the near-wall cycle were illustrated through the significant alteration to the spectral energy distribution downstream of the perturbation. This energetic redistribution,

which involved (i) a displacement of spectral energy away from the location of the near-wall peak, (ii) a subsequent suppression of the near wall peak itself and then (iii) a gradual dissipation of the displaced energy and (iv) a regrowth of the near-wall cycle downstream, was biased towards lower wavelengths, indicating that the impulsive perturbation did not affect the flow bluntly, in all areas of the spectrum, but rather the disruption and recovery of the flow are presumably a strong function of the nature of the perturbation itself – raising the possibility that a perturbation could be 'designed' to achieve particular redistributive goals in the spectral energy organization of the flow. This spectral result was supported by the depression of integral scales in the immediate vicinity of the impulse, and the corresponding non-equilibrium that the impulse engendered in the downstream flow field. The recovery of the near-wall cycle and the dissipation of displaced near-wall structural content were observed to operate on different time scales, consistent with the claim that the stress bore is largely or entirely a local phenomenon.

Finally, the impulse was shown to have a direct impact on discrete structures in the flow field, affecting the location of prograde and retrograde vortex cores and the distribution of aggregate swirl. All of these features of the impulsive perturbation by a roughness strip provide the basic framework for developing methods to alter and control turbulent boundary layers by exploiting the ability of small perturbations to affect vast regions of flow. Of course, a direct measure of wall shear stress would be required in order to make any concrete conclusions about the effect of these perturbations on skin friction. It is also worth noting that the current experiment considered a reasonably large impulse height, despite the small impulse magnitude as measured by the roughness function, and therefore the results perhaps have application to a broader class of problems beyond roughness including perturbation by obstacles.

This work is supported by the Air Force Office of Scientific Research Hypersonics and Turbulence portfolio, under grant #FA9550-08-1-0049 (Program Manager J. Schmisseur). The authors wish to thank C. Gonzalez of California Polytechnic University Pomona for assistance with the PIV setup, as well as M. Guala of the Graduate Aerospace Laboratories at the California Institute of Technology for assistance in preparing the wind tunnel for the current experiments. In addition, the authors thank the reviewers for their very helpful comments, which significantly improved this manuscript.

## REFERENCES

Andreopoulos, J. & Wood, D. H. 1982 The response of a turbulent boundary layer to a short length of surface roughness. *J. Fluid Mech.* **118**, 143–164.

Antonia, R. A. & Luxton, R. E. 1971*a* The response of a turbulent boundary layer to a step change in surface roughness. Part 1. Smooth to rough. *J. Fluid Mech.* **48** (4), 721–761.

Antonia, R. A. & Luxton, R. E. 1971*b* The response of a turbulent boundary layer to an upstanding step change in surface roughness. *Trans. ASME: J. Basic Engng* **93**, 22–34.

Antonia, R. A. & Luxton, R. E. 1972 The response of a turbulent boundary layer to a step change in surface roughness. Part 2. Rough-to-smooth. *J. Fluid Mech.* **53** (4), 737–757.

DeGraaff, D. B. & Eaton, J. K. 2000 Reynolds-number scaling of the flat-plate turbulent boundary layer. *J. Fluid Mech.* **422**, 319–346.

Erm, L. P. & Joubert, P. N. 1991 Low-Reynolds-number turbulent boundary layers. *J. Fluid Mech.* **230**, 1–44.

Freymuth, P. 1977 Frequency response and electronic testing for constant-temperature hot-wire anemometers. *J. Phys.* E*: Sci, Instrum.* **10**, 705.

Hamilton, J. M., Kim, J. & Waleffe, F. 1995 Regeneration mechanisms of near-wall turbulence structures. *J. Fluid Mech.* **287**, 317–348.

Hutchins, N. & Marusic, I. 2007 Large-scale influences in near-wall turbulence. *Phil. Trans. R. Soc. Lond.* **365**, 647–664.

Hutchins, N., Nickels, T. B., Marusic, I. & Chong, M. S. 2009 Hot-wire spatial resolution issues in wall-bounded turbulence. *J. Fluid Mech.* **635**, 103–136.

Jiménez, J. 2004 Turbulent flows over rough walls. *Annu Rev. Fluid Mech.* **36**, 173–196.

Jiménez, J. & Pinelli, A. 1999 The autonomous cycle of near-wall turbulence. *J. Fluid Mech.* **389**, 335–359.

Leonardi, S., Orlandi, P., Smalley, R. J., Djenidi, L. & Antonia, R. A. 2003 Direct numerical simulations of turbulent channel flow with transverse square bars on one wall. *J. Fluid Mech.* **491**, 229–238.

Monty, J. P., Hutchins, N., Ng, H. C. H., Marusic, I. & Chong, M. S. 2009 A comparison of turbulent pipe, channel and boundary layer flows. *J. Fluid Mech.* **632**, 431–442.

Morrison, J. F. 2010 Boundary layers under strong distortion: an experimentalist's view. In *Prediction of Turbulent Flows*, pp. 163–206. Cambridge University Press.

Morrison, J. F., McKeon, B. J., Jiang, W. & Smits, A. J. 2004 Scaling of the streamwise velocity component in turbulent pipe flow. *J. Fluid Mech.* **508**, 99–131.

Pearson, B. R., Elavarasan, R. & Antonia, R. A. 1997 Effect of a short roughness strip on a turbulent boundary layer. *Appl. Sci. Res.* **59**, 61–75.

Smits, A. J. & Wood, D. H. 1985 The response of turbulent boundary layers to sudden perturbations. *Annu. Rev. Fluid Mech.* **17**, 321–358.

Smits, A. J., Young, S. T. B. & Bradshaw, P. 1979 The effect of short regions of high curvature on turbulent boundary layers. *J. Fluid Mech.* **94**, 209–242.

Westerweel, J. 1997 Fundamentals of digital particle image velocimetry. *Meas. Sci. Technol.* **8**, 1379–1392.

Wu, Y. & Christensen, K. T. 2006 Population trends of spanwise vortices in wall turbulence. *J. Fluid Mech.* **568**, 55–76.

Zhou, J., Adrian, R. J., Balachandar, S. & Kendall, T. M. 1999 Mechanisms for generating coherent packets of hairpin vortices in channel flow. *J. Fluid Mech.* **387**, 353–396.